

# Direct observation of turbulent magnetic reconnection in the solar wind

Received: 11 February 2022

Accepted: 30 September 2022

Published online: 10 November 2022

 Check for updates

Rongsheng Wang<sup>1,2</sup>✉, Shimou Wang<sup>1,2</sup>, Quanming Lu<sup>1,2</sup>✉, Xinmin Li<sup>1,2</sup>, San Lu<sup>1,2</sup> & Walter Gonzalez<sup>3</sup>

Magnetic reconnection in a current sheet is commonly found in astrophysical plasma environments. If it is often bursty, releasing magnetic free energy explosively, in planetary magnetospheres, it instead displays a quasi-steady state in the solar wind, where the energy is dissipated via slow-mode shocks. The reason for this difference is elusive. Here we present a direct observation of bursty and turbulent magnetic reconnection in the solar wind, with its associated exhausts bounded by a pair of slow-mode shocks. We infer that the plasma is more efficiently heated in the magnetic reconnection diffusion region than across the shocks and that the flow enhancement is much higher in the exhausts than in the area around the diffusion region. We detected 75 other, similar diffusion-region events in solar wind data between October 2017 and May 2019, suggesting that bursty reconnection in the solar wind is more common than previously thought and actively contributes to solar wind acceleration and heating.

Magnetic reconnection is triggered in the localized diffusion region where the frozen-in field condition of magnetohydrodynamics is violated<sup>1–3</sup>. The diffusion region is frequently observed in the magnetosphere<sup>4–6</sup>; however, detections are lacking in the heliospheric current sheet (HCS)<sup>7–12</sup>, a sprawling surface embedded in the solar wind and extending throughout the entire solar system (Fig. 1a). The absence of the diffusion region in the solar wind challenges the current theory of reconnection and causes controversies on its nature.

The Magnetospheric Multiscale (MMS) mission<sup>13</sup> launched in 2015 was designed to fulfil definitive exploration of electron-scale kinetic physics in the magnetosphere. Fast Plasma Investigation<sup>14</sup> (FPI) onboard the MMS can provide plasma measurements with an unprecedentedly high resolution of 150 ms for ions and 30 ms for electrons. The magnetic<sup>15</sup> and electric field<sup>16,17</sup> data are sampled at 128 s<sup>−1</sup> and at 8,192 s<sup>−1</sup>, respectively. After the first two phases, the MMS apogee has been raised to as far as 25 Earth radii ( $R_E$ ) since October 2017, which has enabled investigation of kinetic physics in the solar wind. Because FPIs are optimized for magnetospheric response, many problems arise when using the FPI data in the solar wind. A few methods have been

proposed to resolve these problems<sup>18,19</sup>. Here we applied a specially designed Hampel filter<sup>18</sup> to mitigate the effects of instrumental artifacts in the solar wind.

## Results

### Overview of the reconnection event

On 10 November 2017, the MMS repeatedly crossed the HCS in the solar wind. Here we focused on the crossings during 09:30–10:10 UT at (9.0, 21.8, 6.8)  $R_E$  in geocentric–solar–ecliptic (GSE) coordinates (Fig. 2). At 09:40 UT, the radial magnetic field  $B_R$  in the radial-tangential-normal coordinates changed polarity from positive to negative (Fig. 2c), accompanied by the switching of super-thermal electrons from 0° to the bidirectional distribution (Fig. 2b), where the fluxes at 180° were higher than those at 0°. At 09:44 UT,  $B_R$  changed polarity again from negative to positive and the electrons turned direction accordingly from the bidirectional distribution to 0°. Since no complete switching of the super-thermal electrons from 0° to 180° or vice versa occurred, the MMS partially crossed the HCS<sup>12</sup> twice during 09:39–09:46 UT.

<sup>1</sup>Deep Space Exploration Laboratory/School of Earth and Space Sciences, University of Science and Technology of China, Hefei, China. <sup>2</sup>CAS Center for Excellence in Comparative Planetology/CAS Key Laboratory of Geospace Environment/Anhui Mengcheng National Geophysical Observatory, University of Science and Technology of China, Hefei, China. <sup>3</sup>China–Brazil Joint Laboratory for Space Weather, Instituto Nacional de Pesquisas Espaciais, São Jose dos Campos, Brazil. ✉e-mail: [rswan@ustc.edu.cn](mailto:rswan@ustc.edu.cn); [qmlu@ustc.edu.cn](mailto:qmlu@ustc.edu.cn)

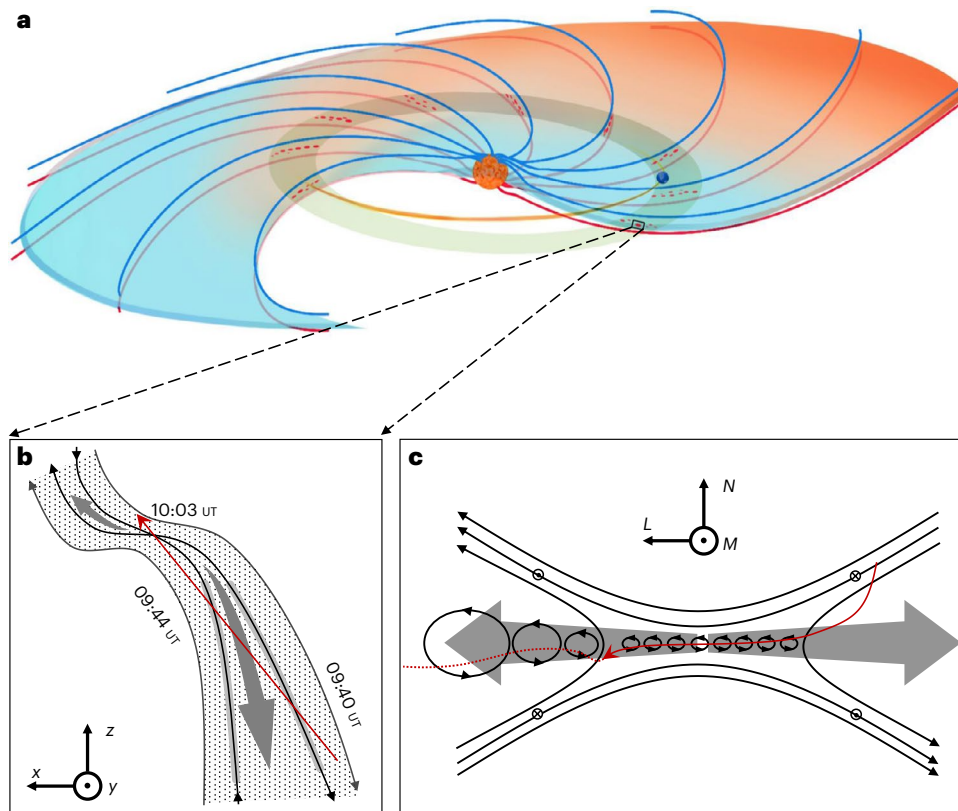


**Fig. 1 | A schematic of the HCS and the reconnection paradigm within it.** **a**, The HCS (red and blue shaded area) encircles the Sun. The solid blue and red lines denote the magnetic field lines pointing out and towards the Sun, respectively. **b**, The reconnection paradigm in GSE coordinates. The grey arrows represent the reconnection outflow jets. The shaded areas bounding the jets denote slow-mode shocks. The dotted region is the plasma sheet. The red lines in

**b** and **c** show the MMS trajectory relative to the reconnection and the black lines with arrows denote magnetic field lines. **c**, The diffusion region with the chain of magnetic flux ropes is displayed in the local current coordinate system. The grey arrows denote the outflow jets. The solid red line shows the trajectory relative to the X-line structure while the dotted red line denotes the trace as the MMS flew over the ropes at the right end of the dotted line.

### Observation of reconnection exhaust

In the partial crossings, the spacecraft observed a bifurcated current sheet and detected a plasma jet of  $\sim 50 \text{ km s}^{-1}$  relative to the background solar wind of  $\sim 650 \text{ km s}^{-1}$  (Fig. 2f). The jet was sub-Alfvénic ( $\sim 0.8v_A$ , where  $v_A$  is Alfvén speed based on  $N = 4.5 \text{ cm}^{-3}$  and  $B = 6 \text{ nT}$ ) and primarily from the negative enhancement of  $x$  component of ion bulk flow  $v_{ix}$ .  $v_{ix}$  was anti-correlated (correlated) with the magnetic field component  $B_z$  on the left (right) edge at  $-09:39:50$  ( $-09:43:30$ ) UT. At both edges, the plasma density (Fig. 2e) and temperatures (Fig. 2g,h) were enhanced while the magnetic field magnitude was depressed. These signatures are consistent with the Petschek reconnection<sup>20</sup>, where the exhausts are bounded by slow-mode shocks<sup>8–11,21</sup> as illustrated in Fig. 1b.

To determine whether the slow-mode shock was present at both edges, the set of Rankine–Hugoniot shock jump conditions and an additional six sets of requirements were examined and all were principally satisfied<sup>22,23</sup> (Methods). Moreover, both slow shocks were near the switch-off limit. Therefore, a Petschek-like reconnection exhaust was observed. Afterwards, the spacecraft was situated in the current sheet and bidirectional flows were occasionally detected (09:54–09:57 UT). This result denotes that the reconnection was continuing<sup>12</sup>.

### Observation of reconnection diffusion region

Starting from 10:03 UT, the MMS partially crossed the current sheet multiple times again and a continuous bidirectional electron distribution was observed.  $B_z$  sharply varied from  $+5$  to  $-4 \text{ nT}$  at  $-10:03:15$  UT while the other two components remained negative (Fig. 2d). This indicates that this current sheet was vertical to the ecliptic plane. Strong

ion shear flows in the  $x$  and  $z$  directions were observed, accompanied by flux enhancements of energetic ions (up to  $26 \text{ keV}$ , Fig. 2a) as well as electrons (up to  $200 \text{ keV}$ ; Fig. 2i,j) and sharp increases in ion and electron temperatures. We investigated these partial crossings in detail (Fig. 3) in the local current coordinate system (LMN) (Methods).

In the partial crossing at  $-10:03:15$  UT (the leftmost vertical dashed line in Fig. 3),  $L$  component ion flow  $v_{iL}$  reversed with respect to a background flow of  $\sim 200 \text{ km s}^{-1}$  (blue trace in Fig. 3d) and normal magnetic field  $B_N$  (red trace in Fig. 3b) reversed simultaneously from negative to positive. The  $v_{iL}$  variation before and after the  $B_N$  reversal point was close to  $30 \text{ km s}^{-1} \approx 0.5v_A$ . At the reversal point of  $v_{iL}$ ,  $B_L$  and  $B_N$ , the current density was significantly enhanced to  $60 \text{ nA m}^{-2}$  (Fig. 3c) while the electron density was considerably reduced (Fig. 3a). The simultaneous reversals of  $v_{iL}$  and  $B_N$  indicate that the MMS passed through one reconnection X-line from one outflow region to the other. Since  $B_L$  varied from  $4 \text{ nT}$  to  $-5 \text{ nT}$ , the MMS passed through the upper-right and lower-left quadrants of the X-line region, as illustrated in Fig. 1c. The depression of  $B_M$  in this interval was consistent with the Hall magnetic field in the first and third quadrants of the diffusion region. Here an ambient magnetic field  $B_g$  of  $\sim 4.0 \text{ nT}$  was detected (green trace in Fig. 3b), corresponding to the guide field. The ratio of  $B_g/B_L$  was  $-1$ . Therefore, it is concluded that an ion diffusion region (IDR) was first observed in the solar wind, with a strong guide field.

$B_L$  was close to zero at the centre of the diffusion region (about at the leftmost vertical dashed line) and both electron and ion temperatures peaked there (Fig. 3e,f). This signifies that the electron diffusion region (EDR) could be detected. Figure 4 shows a zoom-in

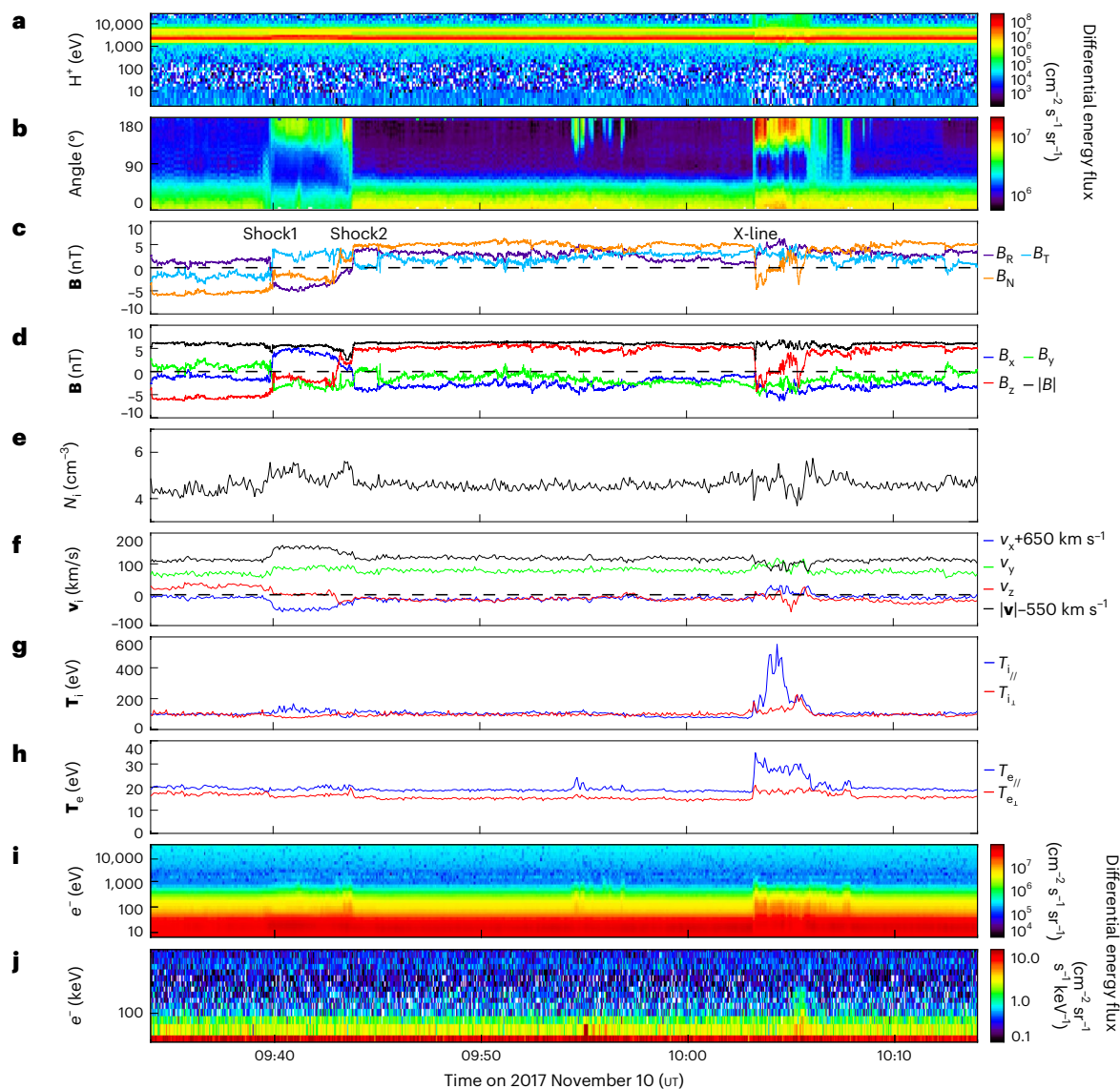


**Fig. 2 | Overview of the reconnection event in the solar wind. a**, Ion energy–time spectrum. **b**, Pitch angle distribution of the electrons with energy between 0.2 and 2 keV. **c**, Magnetic field vector in the radial-tangential-normal coordinates ( $B_R$ , purple;  $B_T$ , light blue;  $B_N$ , orange). **d**, Three components ( $B_x$ , blue;  $B_y$ , green;  $B_z$ , red) and magnitude (black) of the magnetic field in GSE coordinates.

**e**, Proton number density ( $N_i$ ). **f**, Three components ( $v_x$ , blue;  $v_y$ , green;  $v_z$ , red) and intensities (black) of ion bulk flows in GSE coordinates. **g, h**, Ion ( $T_i$ ; **g**) and electron ( $T_e$ ; **h**) temperatures in the parallel (blue) and perpendicular (red) directions. **i, j**, Low (0.1–30 keV; **i**) and high (47–500 keV; **j**) energy–time spectra of electrons.

of the expected EDR. As all four satellites passed through the current sheet (Fig. 4a),  $v_{iL}$  (Fig. 4d) and  $B_N$  (Fig. 4c) changed polarity from negative to positive at 10:03:15 UT. The electron flow  $v_{eL}$  (Fig. 4e) displayed a similar profile to  $v_{iL}$  and the  $v_{eL}$  variation before and after 10:03:15 UT was more than  $100 \text{ km s}^{-1} \approx 1.6 v_A$ , much stronger than  $\delta v_{iL}$  during 10:03:13.5–10:03:16.5 UT (the leftmost shadow area), when the electron flow  $v_{eM}$  (Fig. 4f) was significantly enhanced in the  $-M$  direction. This strong  $v_{eM}$  suggests that the MMS detected the electron current layer (ECL) at the IDR centre.

Inside the ECL, two quadrants of the Hall magnetic field were clear (Fig. 4b). The perpendicular electric field  $E_{\perp N}$  in the frame of background flow was negative while  $B_L > 0$  and basically positive while  $B_L < 0$ , consistent with the Hall electric field<sup>24</sup>. These Hall magnetic and electric fields inside the ECL are similar to previous observations of the Hall field inside the EDR<sup>6,25</sup>. Moreover, the measured electric field departed from  $-(\mathbf{V}_e \times \mathbf{B})$  and  $-(\mathbf{V}_i \times \mathbf{B})$  (Fig. 4g), indicating violation of the electron frozen-in condition. Because of the strong guide field, an intense parallel electric field was concurrently observed (Fig. 4j) as predicted in

simulations<sup>26</sup>. The energy dissipation<sup>27</sup>  $\mathbf{J} \cdot (\mathbf{E} + \mathbf{V}_e \times \mathbf{B})$  was significant (Fig. 4h), where  $\mathbf{J}$  and  $\mathbf{E}$  represent the current density and measured electric field vector, respectively. The electron crescent distribution has been regarded as one typical characteristic for the EDR<sup>4,5,28,29</sup>. The non-gyrotropic electron distribution was indeed detected in the whole interval and the crescent distribution was evident, as shown in Fig. 5a. In the parallel direction, the bidirectional distribution can always be detected (Fig. 5b) and the fluxes in  $v_{e\parallel} < 0$  were higher than those in  $v_{e\parallel} > 0$ , which could be caused by the positive parallel electric field.

All these observations indicate that the ECL is an EDR<sup>4,5,24,25,27,28</sup>. Nevertheless, these observed features were not unique to the EDR, since the simulation<sup>29</sup> found that they existed downstream of the EDR and along the separatrices. In our event, simultaneous reversal of  $B_L$  and  $B_N$  indicates that the MMS crossed the centre of the ion diffusion region, that is, the EDR. Therefore, we concluded that the spacecraft was located inside the EDR during 10:03:13.5–10:03:16.5 UT rather than its extension region. The randomly fluctuating  $\mathbf{J} \cdot (\mathbf{E} + \mathbf{V}_e \times \mathbf{B})$  implies that the reconnection should have evolved into turbulence rather

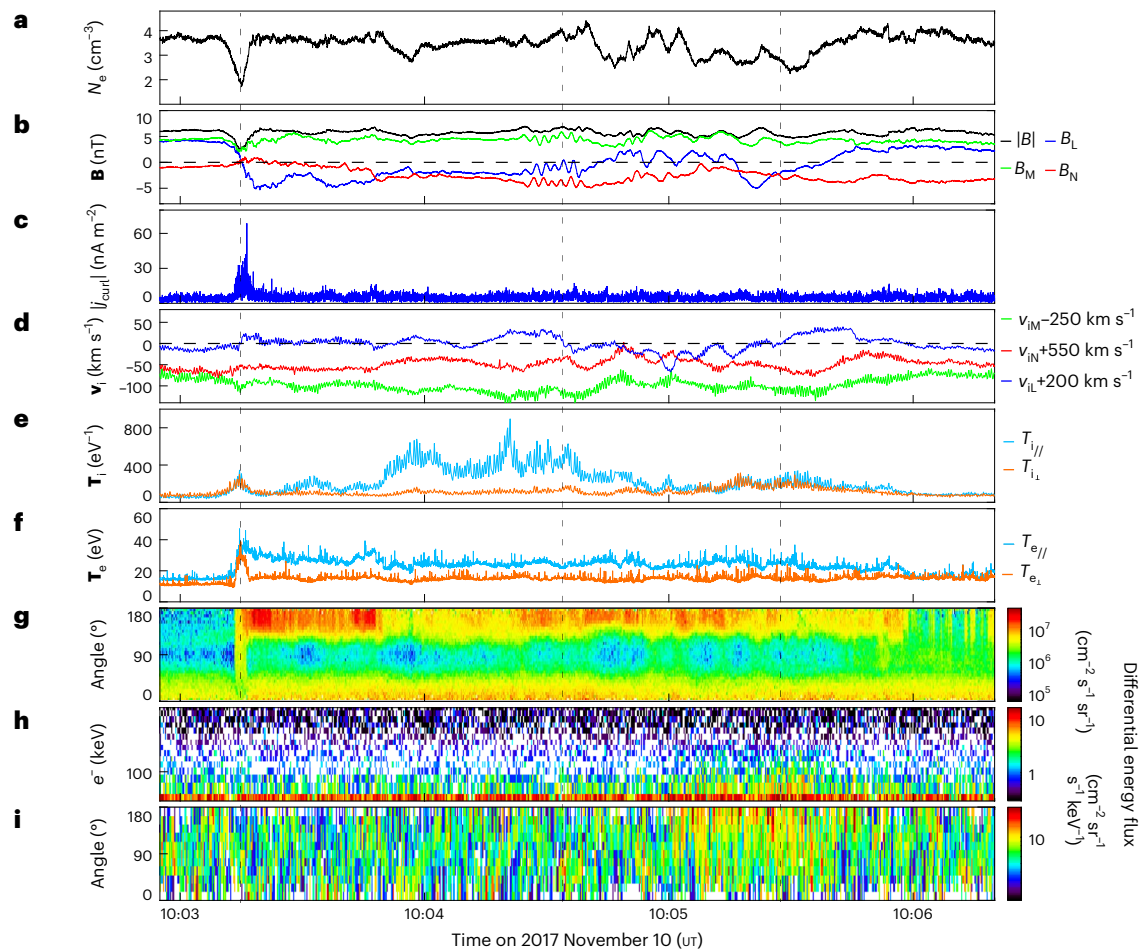


**Fig. 3 | Measurements of turbulent reconnection.** The data are displayed in the local current coordinate system (LMN). The vertical dashed lines correspond to the  $\nu_{IL}$  reversal points. **a**, Electron number density. **b**, Magnetic field vector ( $B_L$ , blue;  $B_M$ , green;  $B_N$ , red) and magnitude (black). **c**, Absolute value of current density from the curlmeter technique. **d**, Three components of ion bulk flows

( $\nu_{IL}$ , blue;  $\nu_{IM}$ , green;  $\nu_{IN}$ , red). **e**, Ion parallel (light blue) and perpendicular (orange) temperatures. **f**, Electron parallel (light blue) and perpendicular (orange) temperatures. **g**, Pitch angle distribution of electrons in the 0.2–2 keV energy range. **h, i**, Differential energy fluxes (**h**) and pitch angle distribution (**i**) of the electrons from 47 to 523 keV.

than the laminar state when  $\mathbf{J} \cdot (\mathbf{E} + \mathbf{V}_e \times \mathbf{B})$  was always positive at the EDR centre<sup>6,25,27</sup>.

Inside the EDR, a series of bipolar  $B_N$  signatures (Fig. 4c) were observed, expanded in Fig. 5. Inside the bipolar  $B_N$  signatures, except for the smallest one at 10:03:14.8 UT,  $B_M$  had a local minimum. These bipolar  $B_N$  signatures before 10:03:14.5 UT overlapped with a background negative  $B_N$ . After that time, the positive reconnected magnetic field  $B_N$  increased gradually and became strong after 10:03:15 UT, and thereby the bipolar  $B_N$  signature became ambiguous. The bipolar  $B_N$  signatures with a significant  $B_M$  corresponded to magnetic flux ropes. The core field was in accord with the Hall magnetic field, consistent with previous observations in the magnetotail<sup>30</sup>. The current density was strengthened inside each flux rope (Fig. 5e), consistent with those observed in the magnetosphere<sup>31–33</sup> and HCS<sup>34–36</sup>. After 10:03:15 UT, the current still displayed filaments but the flux rope disappeared. This indicates that the helical magnetic structures were deformed by the strong reconnected field.

Inside the ropes, the current maxima always deviated from the centres (the vertical dashed lines) and were observed near the edges. This indicates that these flux ropes were probably not created by the tearing mode instability, where the maximum current should be generated at their centres. All three components of the current density ( $\mathbf{j}$ ) changed sign within each flux rope (Fig. 5f).  $j_N$  (red trace) varied from negative to positive at each flux rope centre (the vertical dashed lines),

while  $j_L$  and  $j_M$  varied randomly. It seems that the current was swirling around the flux rope. However, the current vortices were very complicated, unlike the simple swirling circle in the  $L$ – $M$  plane. The close correlation between the flux rope and the disturbed electron bulk flows  $\delta v_e$  (Fig. 5g) indicates that the current inside the flux rope should be carried mainly by the electrons. Near the EDR centre (–10:03:15 UT), the disturbed electron bulk flows were stronger than half of the electron Alfvén speed. Namely, the electron Kelvin–Helmholtz instability was unstable there<sup>37,38</sup>. Thus, the observed flux ropes inside the EDR could be produced by the electron Kelvin–Helmholtz instability.

For each flux rope, there was a slight difference between  $B_N$  at the four satellites. This suggests that their spatial scales were comparable to the spacecraft separation. The flux ropes typically endured for 0.1–0.3 s and were supposed to move with a background flow of 200 km s<sup>–1</sup>; then their sizes in the  $L$  direction were roughly assessed at 20–60 km (5–14  $d_e$ ), where  $d_e = 4.3$  km is the electron inertial length based on the density of 1.5 cm<sup>–3</sup> at the EDR centre (Fig. 3a).

After the EDR, three bipolar  $B_N$  signatures from negative to positive were observed in sequence inside the outflow during 10:03:20–10:03:29 UT and  $B_M$  peaked at the reversal points of  $B_N$  (vertical dashed lines in the second–fourth shadow areas in Fig. 4). These magnetic signatures were consistent with the magnetic flux ropes propagating away from the EDR<sup>30,31,39</sup>, as schematized in Fig. 1c. Their duration varied from 1 to 4 seconds and the spatial scale was evaluated to be

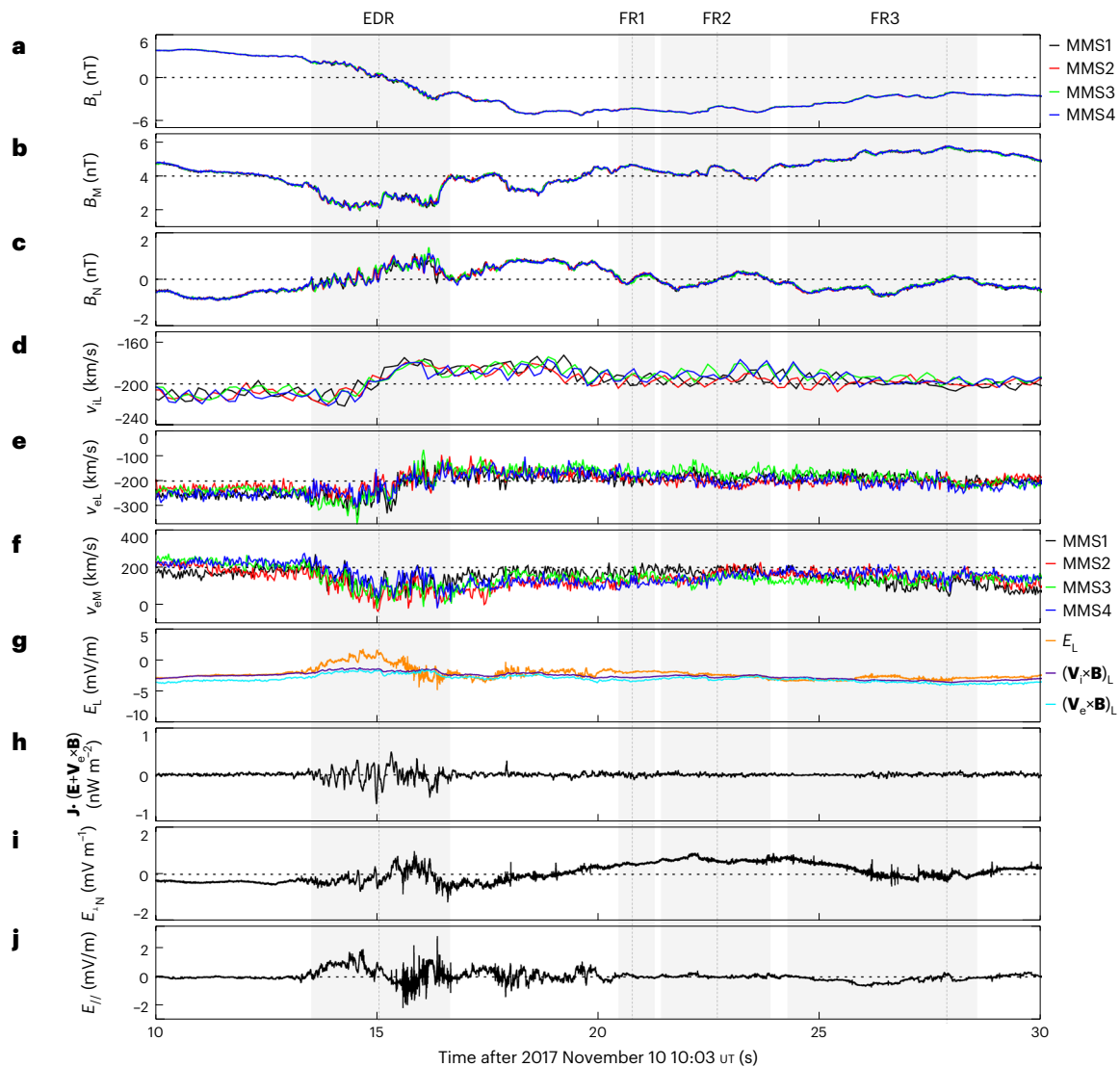


**Fig. 4 | Measurements in the reconnection diffusion region. a–f**, Three components of the magnetic field in the local current coordinate system ( $B_L$ , **a**;  $B_M$ , **b**;  $B_N$ , **c**), ion bulk flow  $v_{iL}$  (**d**) and electron bulk flows  $v_{eL}$  (**e**) and  $v_{eM}$  (**f**) at all four satellites (MMS1, black; MMS2, red; MMS3, green; MMS4, blue). **g**, Electric field  $E_L$  (orange),  $(\mathbf{V}_e \times \mathbf{B})_L$  (light blue) and  $(\mathbf{V}_i \times \mathbf{B})_L$  (purple). **h**, Energy dissipation  $\mathbf{J} \cdot (\mathbf{E} + \mathbf{V}_e \times \mathbf{B})$  in the barycenter of all four satellites. **i, j**, Electric field perpendicular

to local magnetic field in the  $N$  direction (**i**) and parallel electric field (**j**) at MMS1. The leftmost vertical dashed line denotes the reversal point of  $B_L$ . The remaining three vertical dashed lines indicate the  $B_N$  reversal points of the flux ropes. The leftmost shaded region represents the EDR and the other three shaded regions denote the flux ropes (FR1–FR3).

600–2,400 km ( $3\text{--}12 d_i$ ;  $d_i = 186$  km is the ion inertial length), much larger than the spacecraft separation of  $\sim 20$  km. Hence, the magnetic field data at the four satellites (Fig. 4a–c) were almost the same.

These flux ropes were further determined by the three parameters<sup>40,41</sup>: normalized reduced magnetic helicity, cross helicity and residual energy (Methods). The rope sizes inside the EDR were much smaller than those outside of the EDR. The flux rope at 10:03:14.2 UT inside the EDR was composed of two bipolar  $B_N$  signatures without any gap. It seems that these two smaller ropes were coalescing into a larger one. Thus, we speculated that the flux ropes inside the diffusion region indicate that the reconnection had evolved into turbulence, which was further validated by the power-law electric field and magnetic field spectrum therein (Methods).

Inside the EDR, the intense parallel electric field varied gently before 10:03:15 UT and then was strongly perturbed (Fig. 4j), and its average value was approximately  $E_{||} = 0.28$  mV m<sup>-1</sup>. Given the strong guide field, the parallel electric field nearly corresponded to the

reconnection electric field. Then, the reconnection rate  $E_{||}/(v_N B_L - v_L B_N)$  was estimated to be  $\sim 0.25$ . Thus, this event was a fast reconnection and had evolved into a turbulent state. The EDR endured for  $\sim 3$  s with a background speed of 200 km s<sup>-1</sup> in the  $L$  direction, consistent with previous observations of a vertical convection current sheet in the solar wind<sup>42</sup>, and its length was estimated to be 600 km ( $\sim 3.2 d_i$ ). Since the reconnection rate was 0.25, then the EDR half-width was evaluated to be  $\sim 17 d_e$ , which was somewhat thicker than the laminar EDR reported recently<sup>6,25</sup>. As the reconnection evolved into turbulence, the EDR was repeatedly fragmented into flux ropes and filamentary currents and its width continuously broadened<sup>43</sup>. This explains the remarkably wide EDR here.

Both ion (Fig. 3e) and electron (Fig. 3f) temperatures peaked inside the IDR including the parallel and perpendicular components. The energetic ions (Fig. 2a) and the bidirectional electron distribution (Fig. 3g) started to appear in the diffusion region. This denotes that the ions and electrons were energized therein. After the diffusion region, the MMS remained inside the current sheet between 10:03:15 and 10:06

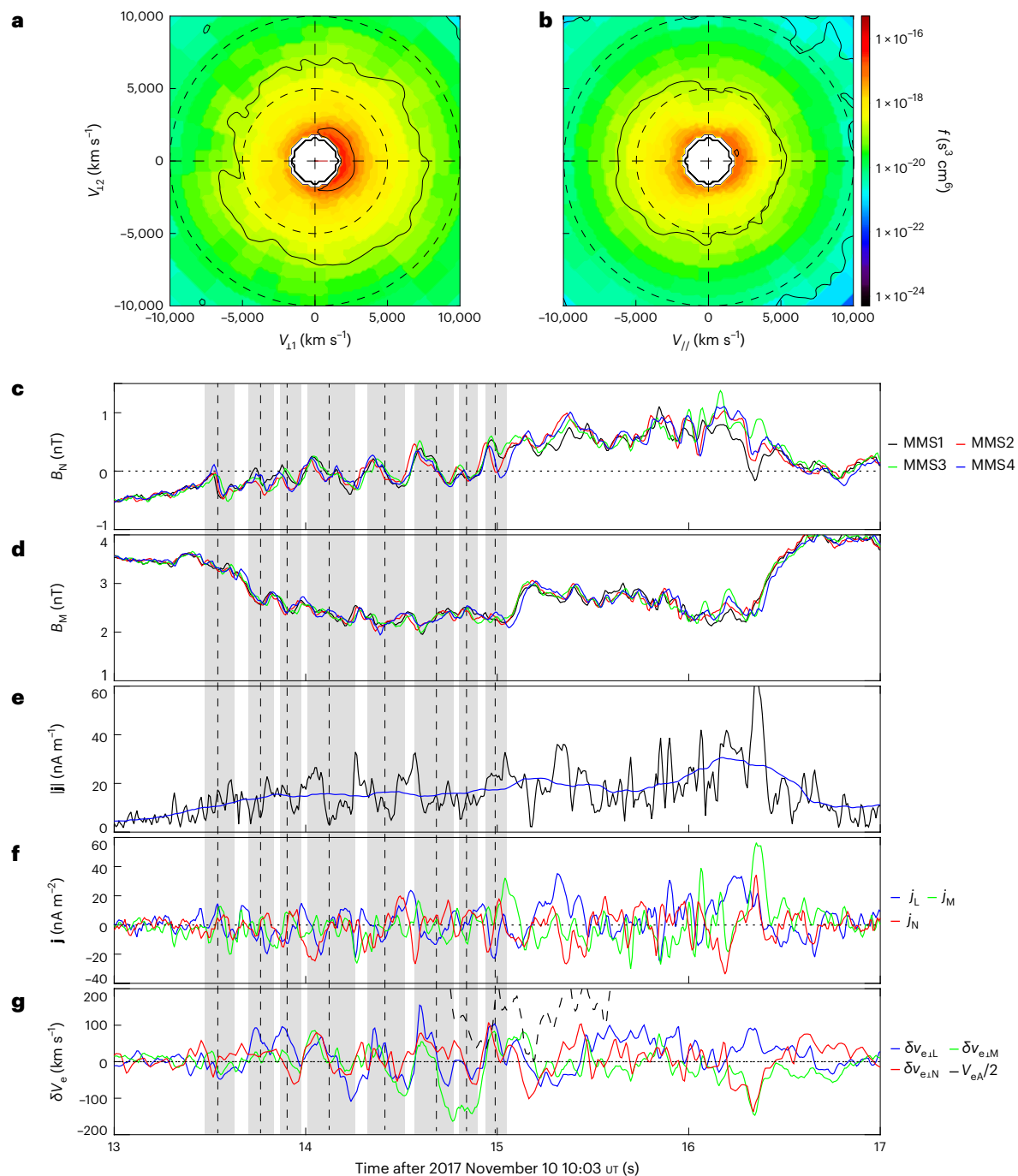


**Fig. 5 | Filamentary currents and magnetic flux ropes inside the electron diffusion region. a, b.** Electron velocity distribution functions in the  $v_{||}$ - $v_{\perp 12}$  (a) and  $v_{||}$ - $v_{\perp 11}$  (b) planes, where  $\mathbf{v}_{\perp 11} = \frac{(\mathbf{B} \times \mathbf{v}_e) \times \mathbf{B}}{B^2}$  and  $\mathbf{v}_{\perp 12} = \frac{\mathbf{B} \times \mathbf{v}_e}{B}$ .  $f$  denotes fluxes. Data are from MMS1 FPI 2017 November 10 10:03:13.965–10:03:13.995 UT. **c, d.**  $B_N$  (c) and  $B_M$  (d) at all four satellites (MMS1, black; MMS2, red; MMS3, green; MMS4,

blue). **e.** Magnitude of current density (black curve) and the average current (blue curve). **f.** Three components of current density. **g.** Disturbed perpendicular electron bulk flow in three directions and half of the electron Alfvén speed (black dashed curve). The vertical shaded areas denote a series of bipolar  $B_N$  signatures and the vertical dashed lines inside them show the centre.

UT (the bidirectional field-aligned electron distribution; Fig. 3g) and detected more  $v_{||}$  reversals, for example, at -10:04:25 and -10:05:28 UT (the second and third vertical dashed lines). At these two sites, the  $v_{||}$  reversal was not coincident with the  $B_L$  reversal and ion temperatures in both the parallel and perpendicular directions ( $T_{i||}$  and  $T_{i\perp}$ , respectively) increased as much as those inside the diffusion region. This implies that reconnection could also occur, but the spacecraft did not directly cross the diffusion regions. In addition to both  $T_{i||}$  and  $T_{i\perp}$  enhancements at the reconnection sites (the three vertical dashed lines),  $T_{i||}$

was significantly enhanced during the whole interval of 10:03–10:06 UT, sometimes even higher than that inside the diffusion region, for example, -10:04:20 UT. Moreover, the parallel electron fluxes were enhanced stably while the antiparallel electron fluxes were intensified violently (Fig. 3g). This means that the current sheet was dynamic and that the electrons and ions were persistently energized. The significant parallel heating was analogous to recent simulations where the strong guide field was found to be crucial for parallel heating<sup>44</sup>. The fluxes of high-energy electrons up to 100 keV were significantly enhanced

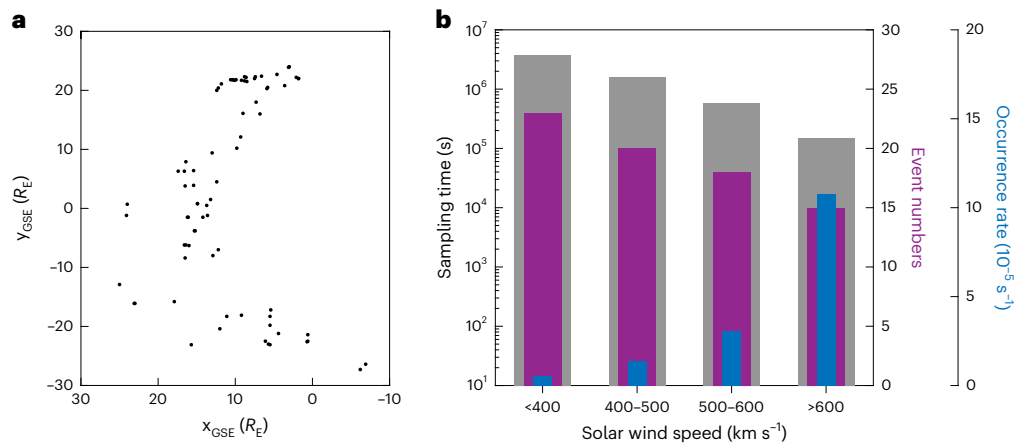


**Fig. 6 | Statistical analysis of the reconnection diffusion region in the solar wind.** Based on MMS observations during October 2017 to May 2019 in the solar wind, we find a total of 76 events where the MMS crossed the reconnection diffusion region from one outflow region to the other. **a**, Locations of all these events in the  $x$ - $y$  plane of the GSE coordinates. **b**, Reconnection events

versus solar wind speed. The solar wind speed was divided into four segments:  $300\text{--}400\text{ km s}^{-1}$ ,  $400\text{--}500\text{ km s}^{-1}$ ,  $500\text{--}600\text{ km s}^{-1}$  and  $600\text{--}700\text{ km s}^{-1}$ . The grey columns represent the sampling time inside the various solar wind speeds. The purple columns show the reconnection event numbers. The blue columns represent the occurrence rate of reconnection.

(Fig. 3h) around the potential reconnection site at  $-10:05:28$  UT and these high-energy electrons were mainly antiparallel to the magnetic field (Fig. 3i), consistent with the electrons between  $0.2$  and  $2$  keV in Fig. 3g. It indicates that the electrons can be directly accelerated to  $100$  keV during magnetic reconnection in the solar wind.

Based on the analysis above, the diffusion region was filled with many magnetic flux ropes and filamentary currents. These flux ropes were rapidly evolving and closely interacting. The plasma was substantially heated during the turbulent reconnection. The protons were accelerated to tens of keV while the electrons were accelerated to  $100$  keV. This kind of turbulent magnetic reconnection is in good agreement with simulations<sup>45,46</sup> and observations in the magnetosphere<sup>30,43</sup>. Far away from the turbulent reconnection site, a Petschek-type exhaust bounded by the slow-mode shock was detected where the plasma was heated and the bulk flow speed was significantly enhanced.

## Discussion

Comparing the plasma heating in the X-line region and Petschek-type exhaust, we find that the heating rate was much larger in the X-line region than across the slow-mode shocks. Although the rate was relatively lower in the slow-mode shocks, the shocks might make a great contribution to the plasma heating since they extended very far. Energetic ions and electrons were only observed around the X-line region other than in the exhaust. Given plenty of flux ropes in the X-line region, their evolution and interaction could be key for the acceleration, as has been suggested by simulations<sup>46–48</sup> and verified by observations<sup>49,50</sup>. The detailed mechanisms are beyond the scope of this paper and will be addressed elsewhere. The bulk flow enhancement was obvious in the exhaust but weaker in the X-line region. Therefore, the form of energy conversion during reconnection was dependent on the distance from the X-line in the solar wind.

By examining the solar wind data during October 2017 to May 2019, we found many current sheet crossings and most of the crossings were associated with the enhanced plasma flows. Based on the criteria of (1) ion bulk flow reversal inside a current sheet, (2) current density enhancement in the current sheets, (3) violation of the ion frozen-in condition, (4) plasma heating and (5) field-aligned bidirectional electron distribution, we recognized a total of 76 events where the MMS traversed the ion diffusion region from one outflow region to the other (Supplementary Table 3) and, among those, 20 instances of the electron

diffusion region. These reconnection diffusion-region events were distributed widely from  $y = -27 R_E$  to  $y = 26 R_E$  (Fig. 6a) and in a variety of solar wind speeds from  $320$  to  $660\text{ km s}^{-1}$  (Fig. 6b). The reconnection events decreased as the solar wind speed increased (purple columns in Fig. 6b). Considering the different sample times at various solar wind speeds (grey columns), we found that the occurrence rate gradually increased as the wind speed grew (blue columns).

Of the 76 reconnection events, 22 were associated with the HCS and other events were observed in localized small-scale current sheets. There were 40 reconnection events where only  $B_{z\text{-GSE}}$  reversal was detected and 17 more events with simultaneous reversals of  $B_{z\text{-GSE}}$  and  $B_{y\text{-GSE}}$  (or  $B_{x\text{-GSE}}$ ). This means that most of the reconnection events (75%) occurred in the vertical current sheet and thus the reconnection outflow was mainly along the  $z$  direction. Moreover, the duration of the diffusion region was generally a few seconds and therefore it is only possible to clearly discern the diffusion region with the plasma data at a time resolution as high as tens of milliseconds. These could be the two main reasons for rare reports on the reconnection diffusion region in the solar wind. The plasma was significantly heated in all the diffusion-region events. However, energetic electrons ( $>50$  keV) were only observed in 6 events and energetic protons ( $>10$  keV) were measured not only in those 6 events but also in 15 other events. Since we focused on the identification of the diffusion region, which was very localized (the duration was a few seconds), it is possible that energetic particles were not detected in most of the events.

In the turbulent fast solar wind, it is expected that a temporal/spatial cascade from large scale to small scale would generate numerous small-scale current sheets where magnetic energy was finally released. Thus, the reconnection can easily be triggered inside these small-scale current sheets, which could be the reason that the reconnection occurrence rate rose sharply in the high-speed solar wind in our statistical analysis. The true occurrence rate was underestimated here because only the diffusion region was considered and reconnection outflow events much more than the diffusion-region events were excluded.

In summary, the reconnection is fast and bursty in the solar wind. The knowledge on reconnection from the magnetosphere is applicable in solar wind as well. The extensively observed Petschek-like exhausts could be extensions of the reconnection X-line region. The reconnection can efficiently energize plasma in the solar wind and might play a role in solar wind heating and acceleration.

## Methods

### Identification of the slow-mode shocks

The shock jump conditions can be verified by the Rankine–Hugoniot (RH) relation and the entropy increases from the upstream to the downstream of the shock. Moreover, six additional sets of requirements for the identification of slow-mode shocks are required. The jump of any physical quantity  $f$  on two sides of the shock can be expressed as  $[f] = f_d - f_u$ , where the subscripts d and u represent the downstream and upstream of the shock.

The RH shock jump conditions are stated as the following:

$$[N_i m_i \tilde{V}_n] = 0 \quad (1)$$

$$[N_i m_i \tilde{V}_n + P_p + 0.5B^2/\mu_0] = 0 \quad (2)$$

$$\left[ N_i m_i \tilde{V}_n \left( \frac{\tilde{V}^2}{2} + 2.5 \frac{P_p}{N_i m_i} + \frac{B^2}{\mu_0 N_i m_i} \right) - \frac{B_n \tilde{\mathbf{V}} \cdot \mathbf{B}}{\mu_0} \right] = 0 \quad (3)$$

$$[B_n] = 0 \quad (4)$$

$$\left[ N_i m_i \tilde{V}_n \tilde{V}_t - \frac{B_n \mathbf{B}_t}{\mu_0} \right] = 0 \quad (5)$$

$$[B_n \tilde{V}_t - \tilde{V}_n \mathbf{B}_t] = 0 \quad (6)$$

where  $N_i$  is the plasma number density,  $m_i$  is proton mass,  $\tilde{V} = V - V_{\text{shock}}$  is the plasma velocity in the shock frame,  $P_p$  is the total plasma pressure and the subscripts n and t denote the normal and tangential components.  $\mu_0$  denotes the permeability of vacuum.

In addition, the following set of slow-mode shock conditions are required from the upstream to the downstream: (1) the total plasma pressure increases, (2) the magnetic pressure decreases, (3) the acute angle  $\theta_B = \arccos(\mathbf{B} \cdot \mathbf{n}/|\mathbf{B}|)$  becomes smaller, where  $\mathbf{n}$  is the shock normal, (4) the upstream intermediate Alfvén Mach number  $M_1 = \tilde{V}_n / (v_A \cos(\theta_B)) \leq 1.0$ , (5) the upstream slow-mode magnetosonic Mach number  $M_{\text{SM}} > 1.0$  and (6) the downstream slow-mode magnetosonic Mach number  $M_{\text{SM}} < 1.0$ ,  $M_{\text{SM}} = \tilde{V}_n / V_{\text{SM}}$ , where

$$V_{\text{SM}} = \tilde{V}_n / \sqrt{\frac{\gamma P_p / (N_i m_i) + v_A^2 - \sqrt{(\gamma P_p / (N_i m_i) + v_A^2)^2 - 4v_A^2 \cos(\theta_B) \gamma P_p / (N_i m_i)}}{2}},$$

$$\gamma = 5/3.$$

In our event, the slow-mode shocks can exist on each side of the exhaust. To recognize the slow-mode shock, the local coordinate system and the reference frame should be determined first. Minimum variance analysis (MVA)<sup>51</sup> and DeHoffmann–Teller analysis<sup>52</sup> were performed for each exhaust side to obtain individual local coordinate and reference frames, respectively. For the leading edge during 09:39–09:41 UT, the MVA method was applied to the magnetic field during 09:39:40–09:40:00 UT at MMS1 with  $L_1 = [0.658, -0.604, 0.450]$ ,  $M_1 = [0.688, 0.725, -0.033]$  and  $N_1 = [-0.306, 0.331, 0.893]$  relative to the GSE coordinates. By the magnetic coplanarity theorem, the normal of shock1 was found to be primarily directed to the minimum variance direction  $N_1$  (less than  $10^\circ$ ) and thus  $N_1$  was used as the shock-normal direction. The DeHoffmann–Teller velocity in the normal direction was regarded as the shock1 velocity. The entropy increasing from the upstream to the downstream was  $-1.79 \times 10^{-24}$  meV K<sup>-1</sup>. The RH relations and other set of requirements are displayed in Supplementary Table 3. As the spacecraft crossed shock1 from the upstream to the downstream, the plasma density (Fig. 1c), plasma pressure and plasma beta increased and magnetic field pressure decreased (Supplementary Fig. 1). The RH

relations (RH1–RH6) were satisfied well (Supplementary Table 1) and the other requirements for the slow-mode shock were also met. Thus, we conclude that a slow-mode shock was observed in the leading edge of the exhaust. In the immediate downstream, the magnetic field was mainly in the normal direction and the tangential component was close to zero, meaning that the slow-mode shock was in the switch-off limit.

A similar analysis was performed on the trailing edge during 09:43–09:45 UT. The local coordinate was  $L_2 = [-0.692, 0.341, 0.637]$ ,  $M_2 = [0.320, -0.646, 0.693]$  and  $N_2 = [0.648, 0.683, 0.337]$  relative to the GSE coordinates. The magnetic coplanarity theorem analysis shows that the normal of shock2 corresponded to the intermediate direction  $M_2$  and thus  $M_2$  was used as the shock-normal direction. The spacecraft crossed shock2 from downstream to upstream (Supplementary Fig. 2) and observed a magnetic flux rope in the downstream at -09:43:12 UT. In this crossing, the plasma pressure was lowered and magnetic pressure was enhanced. The entropy increase from upstream to downstream was  $-1.33 \times 10^{-23}$  meV K<sup>-1</sup>. The RH relations were well satisfied within 15% (Supplementary Table 2) and the other requirements for the slow-mode shock were also met. Furthermore, the magnetic field in the downstream was primarily along the normal direction ( $B_{M_2}$  dominated there). Namely, the slow-mode shock in the trailing edge of the exhaust was switch-off too.

### Determination of the local current coordinate system

The data in the HCS in Fig. 3 are displayed in the local current coordinate system (LMN). These coordinates are obtained from a hybrid method applying to the data at MMS1. The average magnetic field vectors in the two boundary regions of the HCS (10:03:05–10:03:10 UT for one side and 10:03:20–10:03:25 UT for the other side) were labelled as  $\mathbf{B}_1$  and  $\mathbf{B}_2$ , respectively. The normal direction of the current sheet ( $\mathbf{N}$ ) can be obtained by  $\frac{\mathbf{B}_1 \times \mathbf{B}_2}{|\mathbf{B}_1 \times \mathbf{B}_2|}$ . MVA was applied to magnetic field data during 10:03–10:04 UT and maximum variation direction was marked as  $\mathbf{L}_{\text{MVA}}$ . Then,  $\mathbf{M} = \mathbf{N} \times \mathbf{L}_{\text{MVA}}$  and  $\mathbf{L} = \mathbf{M} \times \mathbf{N}$ , with  $\mathbf{L} = (0.312, 0.091, 0.946)$ ,  $\mathbf{M} = (-0.446, -0.862, 0.230)$  and  $\mathbf{N} = (0.836, -0.494, -0.228)$  relative to the GSE coordinates.

### Identification of magnetic flux rope in the solar wind by wavelet analysis

Magnetic flux ropes denote a kind of helical magnetic field structure and generally have a large value of magnetic helicity. They have been extensively investigated in the planetary magnetosphere, interplanetary space and solar corona. In the current sheet of planetary magnetosphere, the flux rope is generally identified by the bipolar signature of magnetic field component normal to the current sheet, accompanied by the peak or valley of the magnetic field component along the current. In the solar wind, the Alfvénic structures have a similar signature to the flux rope<sup>40,53</sup>. Since the Alfvénic structures propagate at the Alfvén speed while the flux ropes represent the magnetic structures, the normalized cross helicity ( $\sigma_c$ ) and residual energy ( $\sigma_r$ ) can be used to distinguish them.

We used the Morlet wavelet analysis as proposed in Telloni et al.<sup>40</sup> and Zhao et al.<sup>41</sup> to investigate the three parameters. The observed magnetic field and plasma flows can be written as follows:  $\mathbf{B} = \mathbf{B}_0 + \mathbf{b}$  and  $\mathbf{V} = \mathbf{V}_0 + \mathbf{u}$ , respectively. Here the subscript of 0 denotes the mean field and  $\mathbf{b}$  and  $\mathbf{u}$  represent the fluctuating variances, respectively. According to Matthaeus et al.<sup>53</sup>, we can get the normalized reduced magnetic field helicity ( $\sigma_m$ ) from a single spacecraft's data as follows:

$$\sigma_m = \frac{2\Im[W_M^*(v, t) \times W_N(v, t)]}{|W_L(v, t)|^2 + |W_M(v, t)|^2 + |W_N(v, t)|^2},$$

where  $W_L$ ,  $W_M$  and  $W_N$  are the wavelet transforms of  $b_L$ ,  $b_M$  and  $b_N$ , respectively;  $W_M^*$  is the complex conjugate of  $W_N$ .  $v$  is frequency associated with the wavelet function. Thus, the handedness of the magnetic field at certain scales/frequencies can be obtained by the spectrogram of

the normalized reduced magnetic helicity. The positive (negative) value of the helicity means right-handed (left-handed) chirality.

The wavelet analysis can also be used to determine the degree of alignment between fluctuating magnetic field and flow field, namely, the cross helicity. The normalized cross helicity can be obtained as follows:

$$\sigma_c = \frac{W^+(u, t) - W^-(u, t)}{W^+(u, t) + W^-(u, t)},$$

where  $W^\pm$  are the sum of the power of the wavelet transforms of the Elsässer variables  $Z^\pm(t) = u \pm \tilde{b}$ ,  $\tilde{b} = \frac{b}{\sqrt{4\pi N_{\text{th}}}}$ . Then, the positive (negative) value of  $\sigma_c$  indicates that more energy resides in the forward (backward) propagating modes with respect to the direction of the mean magnetic field.

The residual energy can be computed as

$$\sigma_r = \frac{W_u(u, t) - W_b(u, t)}{W_u(u, t) + W_b(u, t)},$$

where  $W_u$  and  $W_b$  are the sum of the power of the wavelet transforms of the velocity  $\mathbf{u}$  components and magnetic field  $\mathbf{b}$  components, respectively. This parameter represents the energy difference between the fluctuating kinetic energy and magnetic energy. It is expected to be positive (negative) if the kinetic (magnetic) energy dominates. In general, the flux rope corresponds to a large value of  $|\sigma_m|$ ,  $\sigma_c \approx 0$  and  $\sigma_r < 0$ .

In addition to the typical magnetic field signatures, we used these three parameters to identify the flux ropes reported inside the EDR (Supplementary Fig. 3) and in the reconnection outflows (Supplementary Fig. 4). The results can be found below. The corresponding parameters of the flux ropes are marked by the black oval. At the flux ropes inside the EDR, the helicity was negative and the average value was about  $-0.5$ , the average value of the cross helicity was close to 0 and the residual energy was basically negative, which is consistent with previous observations in the solar wind<sup>53</sup>. As for the first two flux ropes inside the outflows, the negative value of the magnetic helicity was consistent with those inside the EDR. The average value of the cross helicity inside the oval was close to 0 as well. However, the residual energy was positive rather than the expected negative value. One potential explanation is that these tiny flux ropes were observed away from the diffusion region, where the energy was dominated by the kinetic energy. The magnetic helicity inside the EDR and reconnection outflow region are negative. This indicates that the flux ropes are left-handed chirality, consistent with the magnetic field signatures illustrated in Fig. 1c.

### Spectra of magnetic field and electric field intensities in the turbulent reconnection

Fluctuations of magnetic field in the solar wind generally display a typical turbulence power spectrum with an index close to 5/3 (refs. 54–57). In our event, the spectra of magnetic field and electric field intensity over the whole turbulent reconnection region (10:03–10:06 UT) are shown in Supplementary Fig. 5. They exhibit the power-law scaling as well, but a steeper index. The index of the magnetic field and electric field spectra is about 2.34 between the ion cyclotron frequency  $f_{ci}$  and lower hybrid frequency  $f_{lh}$ . It becomes 2.79 for the magnetic field spectrum and 1.63 for the electric field spectrum over  $f_{ci}$ . These observations indicate that the reconnection has led to a well-developed turbulence.

### Data availability

All MMS data are available at <https://lasp.colorado.edu/mms/sdc/public/>.

### Code availability

All the figures were made with the SPEDAS software (Space Physics Environment Data Analysis Software), downloaded from <http://spedas.org/blog/>.

## References

- Vasyliunas, V. M. Theoretical models of magnetic-field line merging. 1. *Rev. Geophys.* **13**, 303–336 (1975).
- Ji, H. T. et al. Magnetic reconnection in the era of exascale computing and multiscale experiments. *Nat. Rev. Phys.* **4**, 263–282 (2022).
- Lu, Q. M., Fu, H. S., Wang, R. S. & Lu, S. Collisionless magnetic reconnection in the magnetosphere. *Chin. Phys. B.* **31**, 089401 (2022).
- Burch, J. L. et al. Electron-scale measurements of magnetic reconnection in space. *Science* **352**, aaf2939 (2016).
- Wang, R. S. et al. Electron-scale quadrants of the hall magnetic field observed by the Magnetospheric Multiscale spacecraft during asymmetric reconnection. *Phys. Rev. Lett.* **118**, 175101 (2017).
- Torbert, R. B. et al. Electron-scale dynamics of the diffusion region during symmetric magnetic reconnection in space. *Science* **362**, 1391–1395 (2018).
- Wei, F. S., Hu, Q., Feng, X. S. & Fan, Q. L. Magnetic reconnection in interplanetary space. *Space Sci. Rev.* **107**, 107–110 (2003).
- Gosling, J. T., Skoug, R. M., McComas, D. J. & Smith, C. W. Direct evidence for magnetic reconnection in the solar wind near 1 AU. *J. Geophys. Res. Space Phys.* **110**, A01107 (2005).
- Phan, T. D. et al. A magnetic reconnection X-line extending more than 390 Earth radii in the solar wind. *Nature* **439**, 175–178 (2006).
- Lavraud, B. et al. Observation of a complex solar wind reconnection exhaust from spacecraft separated by over 1,800  $R_E$ . *Sol. Phys.* **256**, 379–392 (2009).
- Mistry, R., Eastwood, J. P., Phan, T. D. & Hietala, H. Statistical properties of solar wind reconnection exhausts. *J. Geophys. Res. Space Phys.* **122**, 5895–5909 (2017).
- Phan, T. D. et al. Prevalence of magnetic reconnection in the near-Sun heliospheric current sheet. *Astron. Astrophys.* **650**, A13 (2021).
- Burch, J. L., Moore, T. E., Torbert, R. B. & Giles, B. L. Magnetospheric Multiscale overview and science objectives. *Space Sci. Rev.* **199**, 5–21 (2016).
- Pollock, C. et al. Fast Plasma Investigation for Magnetospheric Multiscale. *Space Sci. Rev.* **199**, 331–406 (2016).
- Russell, C. T. et al. The Magnetospheric Multiscale magnetometers. *Space Sci. Rev.* **199**, 189–256 (2016).
- Ergun, R. E. et al. The axial double probe and fields signal processing for the MMS Mission. *Space Sci. Rev.* **199**, 167–188 (2016).
- Lindqvist, P. A. et al. The spin-plane double probe electric field instrument for MMS. *Space Sci. Rev.* **199**, 137–165 (2016).
- Bandyopadhyay, R. et al. Solar wind turbulence studies using MMS Fast Plasma Investigation data. *Astrophys. J.* **866**, 81 (2018).
- Roberts, O. W. et al. A study of the solar wind ion and electron measurements from the Magnetospheric Multiscale Mission's Fast Plasma Investigation. *J. Geophys. Res. Space Phys.* **126**, e2021JA029784 (2021).
- Forbes, T. G. The nature of Petschek-type reconnection. *Earth Planets Space* **53**, 423–429 (2001).
- Phan, T. D. et al. Parker Solar Probe in situ observations of magnetic reconnection exhausts during encounter 1. *Astrophys. J. Suppl. Ser.* **246**, 34 (2020).
- Eriksson, S. et al. Walen and slow-mode shock analyses in the near-Earth magnetotail in connection with a substorm onset on 27 August 2001. *J. Geophys. Res. Space Phys.* **109**, A10212 (2004).
- Sonnerup, B. U. O., Hasegawa, H., Denton, R. E. & Nakamura, T. K. M. Reconstruction of the electron diffusion region. *J. Geophys. Res. Space Phys.* **121**, 4279–4290 (2016).
- Shay, M. A., Drake, J. F., Denton, R. E. & Biskamp, D. Structure of the dissipation region during collisionless magnetic reconnection. *J. Geophys. Res. Space Phys.* **103**, 9165–9176 (1998).

25. Wang, R. S. et al. An electron-scale current sheet without bursty reconnection signatures observed in the near-Earth tail. *Geophys. Res. Lett.* **45**, 4542–4549 (2018).
26. Egedal, J. et al. Cluster observations of bidirectional beams caused by electron trapping during antiparallel reconnection. *J. Geophys. Res. Space Phys.* **115**, A03214 (2010).
27. Zenitani, S., Hesse, M., Klimas, A., Black, C. & Kuznetsova, M. The inner structure of collisionless magnetic reconnection: the electron-frame dissipation measure and Hall fields. *Phys. Plasmas* **18**, 122108 (2011).
28. Hesse, M., Aunai, N., Sibeck, D. & Birn, J. On the electron diffusion region in planar, asymmetric, systems. *Geophys. Res. Lett.* **41**, 8673–8680 (2014).
29. Shay, M. A. et al. Kinetic signatures of the region surrounding the X line in asymmetric (magnetopause) reconnection. *Geophys. Res. Lett.* **43**, 4145–4154 (2016).
30. Wang, R. et al. Coalescence of magnetic flux ropes in the ion diffusion region of magnetic reconnection. *Nat. Phys.* **12**, 263–267 (2016).
31. Slavin, J. A. et al. Geotail observations of magnetic flux ropes in the plasma sheet. *J. Geophys. Res. Space Phys.* **108**, 1015 (2003).
32. Wang, R. S. et al. Electrostatic and electromagnetic fluctuations detected inside magnetic flux ropes during magnetic reconnection. *J. Geophys. Res. Space Phys.* **121**, 9473–9482 (2016).
33. Stawarz, J. E. et al. Intense electric fields and electron-scale substructure within magnetotail flux ropes as revealed by the Magnetospheric Multiscale Mission. *Geophys. Res. Lett.* **45**, 8783–8792 (2018).
34. Moldwin, M. B., Ford, S., Lepping, R., Slavin, J. & Szabo, A. Small-scale magnetic flux ropes in the solar wind. *Geophys. Res. Lett.* **27**, 57–60 (2000).
35. Cartwright, M. L. & Moldwin, M. B. Comparison of small-scale flux rope magnetic properties to large-scale magnetic clouds: evidence for reconnection across the HCS? *J. Geophys. Res. Space Phys.* **113**, A09105 (2008).
36. Wu, D. J., Feng, H. Q. & Chao, J. K. Energy spectrum of interplanetary magnetic flux ropes and its connection with solar activity. *Astron. Astrophys.* **480**, L9–L12 (2008).
37. Fermo, R. L., Drake, J. F. & Swisdak, M. Secondary magnetic islands generated by the Kelvin–Helmholtz instability in a reconnecting current sheet. *Phys. Rev. Lett.* **108**, 255005 (2012).
38. Huang, C. et al. Development of turbulent magnetic reconnection in a magnetic island. *Astrophys. J.* **835**, 245 (2017).
39. Chen, L. J. et al. Observation of energetic electrons within magnetic islands. *Nat. Phys.* **4**, 19–23 (2008).
40. Telloni, D., Bruno, R., D’Amicis, R., Pietropaolo, E. & Carbone, V. Wavelet analysis as a tool to localize magnetic and cross-helicity events in the solar wind. *Astrophys. J.* **751**, 19 (2012).
41. Zhao, L. L. et al. Detection of small magnetic flux ropes from the third and fourth Parker Solar Probe encounters. *Astron. Astrophys.* **650**, A12 (2021).
42. Vörös, Z. et al. Magnetic reconnection within the boundary layer of a magnetic cloud in the solar wind. *J. Geophys. Res. Space Phys.* **126**, e2021JA029415 (2021).
43. Li, X. M. et al. Three-dimensional network of filamentary currents and super-thermal electrons during magnetotail magnetic reconnection. *Nat. Commun.* **13**, 3241 (2022).
44. Shay, M. A. et al. Electron heating during magnetic reconnection: a simulation scaling study. *Phys. Plasmas* **21**, 122902 (2014).
45. Daughton, W. et al. Role of electron physics in the development of turbulent magnetic reconnection in collisionless plasmas. *Nat. Phys.* **7**, 539–542 (2011).
46. Zank, G. P., le Roux, J. A., Webb, G. M., Dosch, A. & Khabarova, O. Particle acceleration via reconnection processes in the supersonic solar wind. *Astrophys. J.* **797**, 28 (2014).
47. Drake, J. F., Swisdak, M., Schoeffler, K. M., Rogers, B. N. & Kobayashi, S. Formation of secondary islands during magnetic reconnection. *Geophys. Res. Lett.* **33**, L13105 (2006).
48. Che, H. & Zank, G. P. Electron acceleration from expanding magnetic vortices during reconnection with a guide field. *Astrophys. J.* **889**, 11 (2020).
49. Zhao, L. L. et al. An unusual energetic particle flux enhancement associated with solar wind magnetic island dynamics. *Astrophys. J. Lett.* **864**, L34 (2018).
50. Zhao, L. L. et al. Particle acceleration at 5 AU associated with turbulence and small-scale magnetic flux ropes. *Astrophys. J.* **872**, 4 (2019).
51. Sonnerup, B. U. & Cahill, L. J. Magnetopause structure and attitude from Explorer 12 observations. *J. Geophys. Res.* **72**, 171–183 (1967).
52. Sonnerup, B. U. O., Papamastorakis, I., Paschmann, G. & Luhr, H. Magnetopause properties from Amptel/Irm observations of the convection electric field: method development. *J. Geophys. Res. Space Phys.* **92**, 12137–12159 (1987).
53. Matthaeus, W. H., Goldstein, M. L. & Smith, C. Evaluation of magnetic helicity in homogeneous turbulence. *Phys. Rev. Lett.* **48**, 1256–1259 (1982).
54. Bruno, R. & Carbone, V. The solar wind as a turbulence laboratory. *Living Rev. Sol. Phys.* **10**, 2 (2013).
55. Bruno, R. et al. The low-frequency break observed in the slow solar wind magnetic spectra. *Astron. Astrophys.* **627**, A96 (2019).
56. Matthaeus, W. H. et al. Density and magnetic field signatures of interplanetary 1/f noise. *Astrophys. J.* **657**, L121–L124 (2007).
57. Tu, C. Y. & Marsch, E. MHD structures, waves and turbulence in the solar-wind: observations and theories. *Space Sci. Rev.* **73**, 1–210 (1995).

## Acknowledgements

This work is supported by the B-type Strategic Priority Program of the Chinese Academy of Sciences (XDB41000000; R.W.), the National Science Foundation of China (NSFC) (grants 41922030 and 42174187; R.W.), the key research programme of frontier sciences CAS (QYZDJ-SSW-DQC010; Q.L.), the Fundamental Research Funds for the Central Universities (R.W.) and the China-Brazil Joint Laboratory for Space Weather and the NSSC/CAS (W.G.). R.W. thanks O. Roberts and R. Nakamura of the Space Research Institute of the Austrian Academy of Sciences for fruitful discussion.

## Author contributions

R.W. carried out the spacecraft data analysis and interpretation and wrote the manuscript. S.W. and X.L. dealt with part of the spacecraft data and took part in the discussion. Q.L. supervised the work and provided the theoretical analysis. X.L. and S.L. took part in the discussion and gave valuable suggestions. W.G. gave valuable suggestions and comments. All the authors discussed the results and commented on the paper.

## Competing interests

The authors declare no competing interests.

## Additional information

**Supplementary information** The online version contains supplementary material available at <https://doi.org/10.1038/s41550-022-01818-5>.

**Correspondence and requests for materials** should be addressed to Rongsheng Wang or Quanming Lu.

**Peer review information** *Nature Astronomy* thanks Lingling Zhao, Rungployphan Kieokaew and Zoltan Vörös for their contribution to the peer review of this work.

**Reprints and permissions information** is available at [www.nature.com/reprints](http://www.nature.com/reprints).

**Publisher's note** Springer Nature remains neutral with regard to jurisdictional claims in published maps and institutional affiliations.

Springer Nature or its licensor (e.g. a society or other partner) holds exclusive rights to this article under a publishing agreement with the author(s) or other rightsholder(s); author self-archiving of the accepted manuscript version of this article is solely governed by the terms of such publishing agreement and applicable law.

© The Author(s), under exclusive licence to Springer Nature Limited 2022